Earthquakes and Structures, *Vol. 18, No. 5 (2020)581-598*
DOI: https://doi.org/10.12989/eas.2020.18.5.581

Seismic analysis of RC tubular columns in air-cooled supporting structure of TPP

Bo Wang[1], Ke Yang[1], Huijuan Dai[2], Guoliang Bai[3] and Chaogang Qin*[1]

[1]School of Civil Engineering, Chang'an University, Xi'an 710061, China
[2]School of Civil Engineering, Xi'an University of Science and Technology, Xi'an 710054, China
[3]School of Civil Engineering, Xi'an University of Architecture and Technology, Xi'an 710055, China

(Received December 24, 2019, Revised April 20, 2020, Accepted April 21, 2020)

Abstract. This paper aims to investigate the seismic behavior and influence parameters of the large-scaled thin-walled reinforced concrete (RC) tubular columns in air-cooled supporting structures of thermal power plants (TPPs). Cyclic loading tests and finite element analysis were performed on 1/8-scaled specimens considering the influence of wall diameter ratio, axial compression ratio, longitudinal reinforcement ratio, stirrup reinforcement ratio and adding steel diagonal braces (SDBs). The research results showed that the cracks mainly occurred on the lower half part of RC tubular columns during the cyclic loading test; the specimen with the minimum wall diameter ratio presented the earlier cracking and had the most cracks; the failure mode of RC tubular columns was large bias compression failure; increasing the axial compression ratio could increase the lateral bearing capacity and energy dissipation capacity, but also weaken the ductility and aggravate the lateral stiffness deterioration; increasing the longitudinal reinforcement ratio could efficiently enhance the seismic behavior; increasing the stirrup reinforcement ratio was favorable to the ductility; RC tubular columns with SDBs had a much higher bearing capacity and lateral stiffness than those without SDBs, and with the decrease of the angle between columns and SDBs, both bearing capacity and lateral stiffness increased significantly.

Keywords: thermal power plant (TPP); RC tubular column; seismic behavior; cyclic loading test; parametric analysis

1. Introduction

In the past, the build location of thermal power plants (TPPs) is restricted by water resource since the conventional cooling technique depends directly on the water. With the development of technology, a novel cooling technique named direct air-cooled system has been invented, which is widely adopted for TPPs in water-deficient regions (Odabaee and Hooman 2011, O'Donovan and Grimes 2014, Bustamante *et al*. 2015). So as to support air-cooled condensers in the direct air-cooled system, several supporting structural systems have been developed, such as steel braced frame structure, reinforced concrete (RC) frame structure, steel solid web girder-RC tubular column structure, steel truss-RC tubular column structure, steel braced truss-RC tubular column structure and so forth. Among them, the latter two types of structural systems have been widely applied in TPPs with large-capacity units over 600 MW, as shown in Fig. 1. Fig. 2 shows the schematics of these two structural systems with main dimensional characteristics. In general, there is an array of large-scale thin-walled RC tubular columns under the spacial steel truss platform to support upper A-shaped steel frames and technological equipment. The steel braced truss-RC tubular column structure is a novel supporting structure with larger seismic capacity compared to the traditional steel truss-RC tubular column structure, in which steel diagonal braces (SDBs) are used to connect the corbels of RC tubular columns and the lower chords of steel truss.

Recently, the overall seismic performance of these two steel truss-RC tubular column hybrid structures has been studied based on pseudo-dynamic tests and numerical analysis (Jiang *et al*. 2011, Wang *et al*. 2018, 2019). The research results indicated that this kind of hybrid supporting structure has the sufficient ductility and good energy dissipation capacity to satisfy the seismic requirements in strong earthquake prone regions. However, it is a single aseismic fortification structural system, and RC tubular columns are the main energy dissipation components which directly affect the safety and reliability of the whole supporting structure. Accordingly, it is necessary to investigate the seismic behavior of RC tubular columns on the basis of the whole structural analysis. In last decades, several researches regarding RC hollow columns were carried out (Mokrin 1988, Tayem and Najmi 1996, Yeh *et al*. 2002, Han *et al*. 2014, Lee *et al*. 2015), however, most of them focused on bridge piers with rectangle or circle hollow sections in the field of highway engineering whose characteristics are different from the RC tubular columns in air-cooled supporting structures. Due to the production and functional requirements in TPPs, RC tubular columns in air-cooled supporting structures always have large size and bear heavy loads caused by the upper truss platform and equipment. The height of column is above 30~50 m. The external diameter of column is about 4~5 m, while the wall

*Corresponding author, Lecturer
E-mail: qinchaogang@chd.edu.cn

http://www.techno-press.com/journals/was&subpage=7
ISSN: 2092-7614 (Print), 2092-7622 (Online)

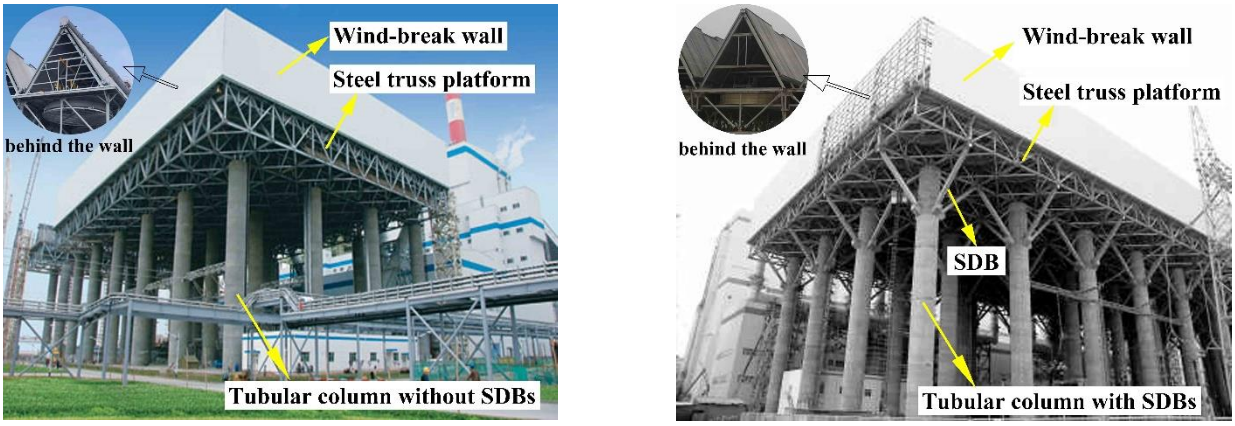

(a) Traditional supporting structure (b) Novel supporting structure

Fig. 1 Practical photos of two types of steel truss-RC tubular column supporting structures

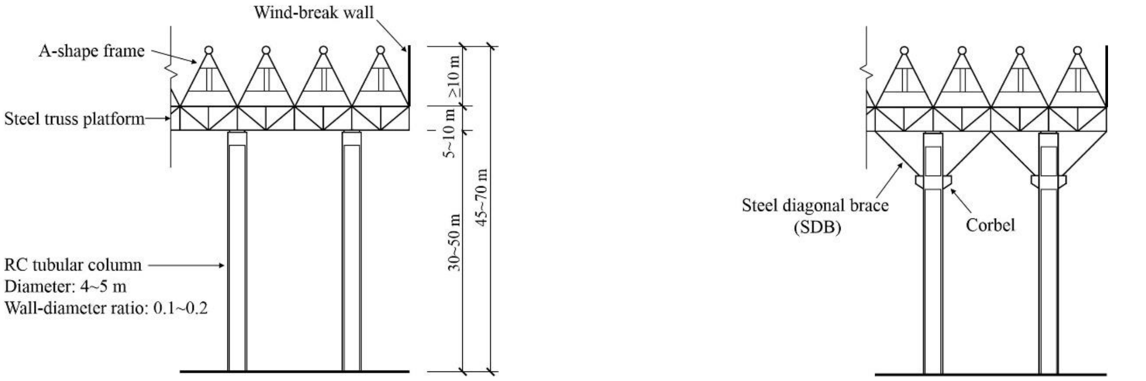

(a) Traditional supporting structure without SDBs (b) Novel supporting structure with SDBs

Fig. 2 Schematic diagrams of two types of steel truss-RC tubular column supporting structures

thickness is only about 1/10~1/5 of the external diameter, as shown in Fig. 2(a).

In this study, the seismic behavior and its influence parameters of RC tubular columns in air-cooled supporting structures of TPPs were investigated. Firstly, cyclic loading tests on three 1/8 scaled specimens were conducted. Then, the finite element modeling approaches were validated by the cyclic loading tests results. Finally, parametric analysis was made based on the experimental results and finite element analysis (FEA) of numerical models with variable parameters including axial compression ratio, longitudinal reinforcement ratio, stirrup reinforcement ratio and adding SDBs.

2 Experimental program and results

2.1 Experimental program

2.1.1 Test specimens

RC tubular column in a practical air-cooled supporting structure of TPPs located in high seismic region of China was taken as the prototype. According to the China seismic design code (GB 50011-2010, 2016), the seismic precautionary intensity is 8-degree with the peak ground acceleration (PGA) of 0.20 g. The site condition is class II.

The height, external diameter and wall thickness of the prototype column was 40 m, 4 m and 0.4 m, respectively. Considering the limitation of test field, the model scale factor for length was determined as 1/8. The external diameter and wall thickness of specimen were 500 mm and 50 mm, respectively. It is noted that the theoretical height of specimen calculated by scale factor was 5 m. However, due to the restraint of laboratory conditions, the actual height of the specimen was taken as 3070 mm. Although the corresponding slenderness ratio was reduced, the specimens still belong to the long column. There is no essential difference in stress mechanism, failure pattern and seismic behavior between the prototype and specimens. In addition, since the wall thickness of specimen is too small, in order to ensure construction quality, longitudinal steel rebars were arranged in a single row and distributed evenly in the annular section of specimens, resulting in a single layer stirrups in specimens.

The wall diameter ratio, axial compression ratio and longitudinal reinforcement ratio were selected as variable parameters of specimens. The designed parameters of specimens are shown in Table 1. Fig. 3 shows the dimensions and steel reinforcement details of three specimens. For the convenience of loading, the top 300 mm of specimens was designed as rectangular section.

Table 1 Design parameters of specimens

Specimen	External diameter (mm)	Internal diameter (mm)	Wall thickness (mm)	Wall diameter ratio	Axial compression ratio	Longitudinal reinforcement ratio
TC-0.1	500	400	50	0.10	0.14	1.66%
TC-0.14	500	360	70	0.14	0.20	1.66%
TC-0.2	500	300	100	0.20	0.14	1.00%

*TC: Tubular Column; the number 0.1, 0.14 and 0.2 following "TC": wall diameter ratios of specimens

Table 2 Material properties of specimens

Material	Diameter (mm)	Strength grade	Yield strength f_y (MPa)	Ultimate strength f_u (MPa)	Yield strain ε_y (με)	Elastic modulus E_s (MPa)
Steel rebar	8	HPB235	315.9	506.7	1524.9	207120
	10	HRB400	461.7	688.3	2115.1	218268
Concrete	Specimen number	Strength grade	$f_{cu,k}$ (MPa)	f_{ck} (MPa)	f_c (MPa)	Elastic modulus E_c (MPa)
	TC-0.1	C40	38.1	25.5	18.2	28083.7
	TC-0.14	C40	46.4	31.1	22.0	30159.0
	TC-0.2	C40	42.0	28.1	20.1	29113.1

*$f_{cu,k}$: the standard value of cube compressive strength of concrete; f_{ck}: the standard value of axial compressive strength of concrete; f_c: the design value of axial compressive strength of concrete

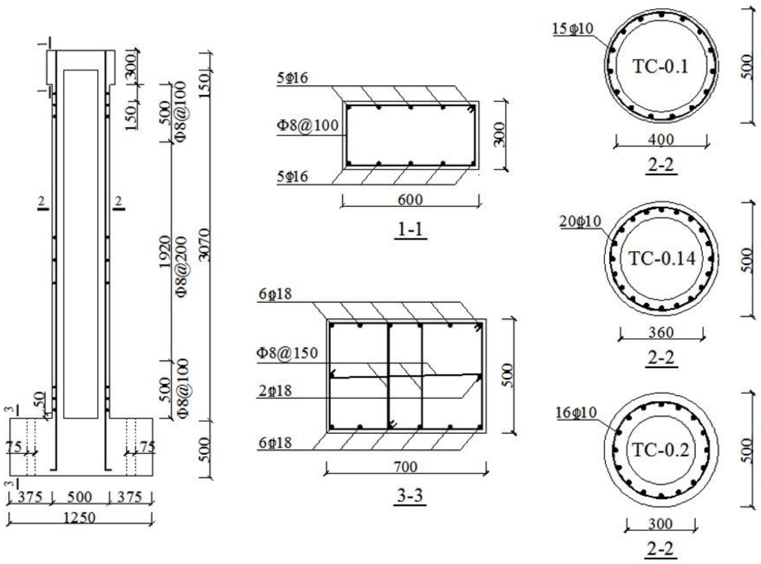

Fig. 3 Dimensions and steel reinforcement details of specimens (Unit: mm)

Moreover, the top 150 mm of specimen was cast with solid section to avoid the local compression failure. The bottom of specimens was fixed to the rigid base. Table 2 provides the test material properties of specimens.

2.1.2 Loading program

Fig. 4 shows the test setup and instrumentation of specimens subjected to a constant axial load and cycling lateral load. The axial load was applied by a hydraulic jack which can move laterally together with the specimen. The lateral load with displacement control method was applied to the top of the specimen by hydraulic actuator fixed to the reaction wall. Displacement meters were laterally installed at the top, 1/3 and 2/3 height of the specimen. Strain gauges were mounted on longitudinal steel rebars and stirrups at the bottom of the specimens, measuring steel strains during the tests (Fig. 4).

The axial loads of specimens TC-0.1, TC-0.14 and TC-0.2 determined by axial compression ratio were 180 kN, 420 kN and 360 kN, respectively. Cyclic loading tests conducted in this paper were aiming to investigate the damage characteristics and failure mechanism of RC tubular columns. Parameter analysis on seismic behavior of RC tubular columns was carried out through the simulation method based on the test results. Therefore, differed from conventional loading sequences with the constant value of displacement increment and cycle number (Tsonos 2007, 2014, Kakaletsis *et al*. 2011), an exploratory lateral loading protocol was adopted for this special RC tubular column, as shown in Fig. 5(a).

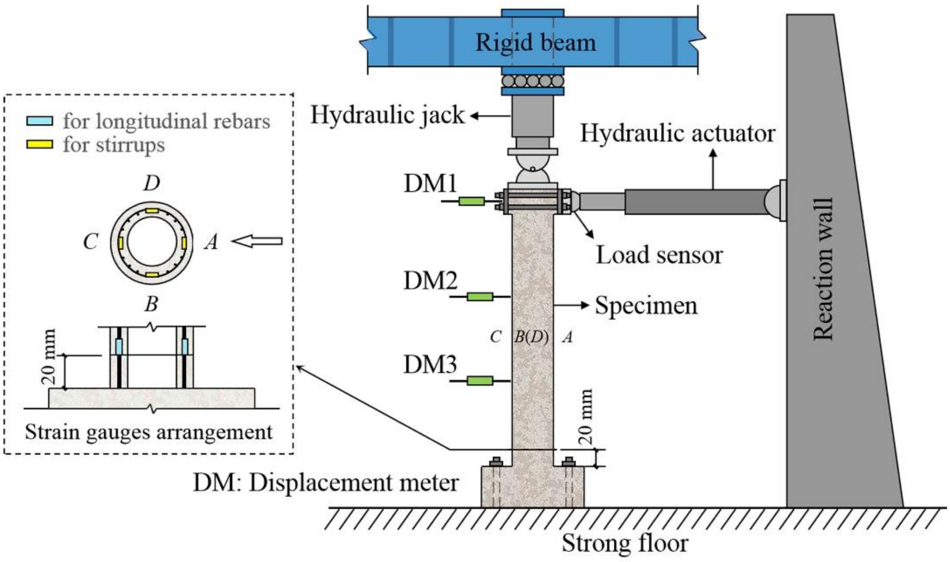

Fig. 4 Test setup and instrumentation

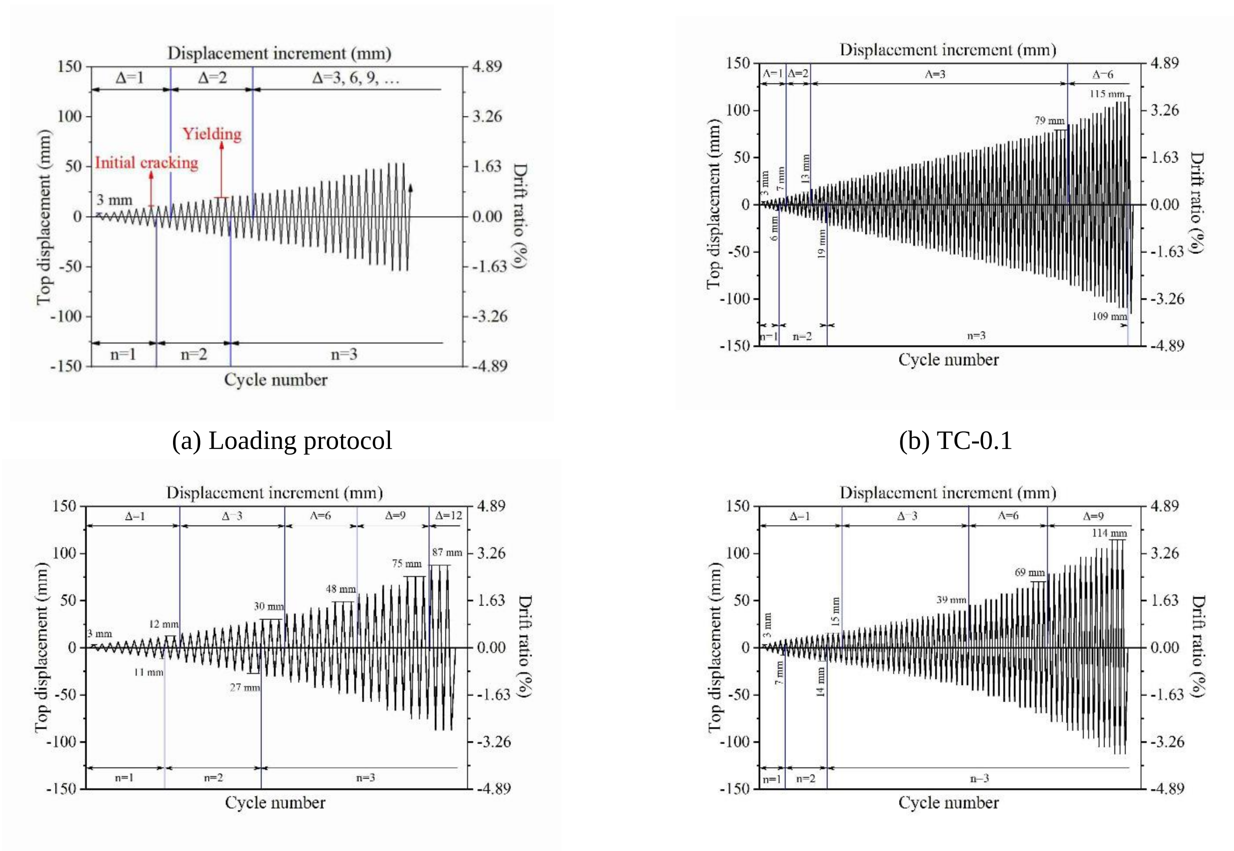

(a) Loading protocol (b) TC-0.1

(c) TC-0.14 (d) TC-0.2

Fig. 5 Loading protocols of specimens

3-mm initial cyclic lateral displacement was exerted through the MTS actuator at first. Then, the value of the target displacement increased with increment of 1 mm each cycle until visible cracks were observed on the specimens. The displacement increment value and the cycle number then increased to 2 mm and 2 times until the tensile longitudinal steel rebars yielded. After that, the displacement increment value and the cycle number were adjusted as 3 mm, 6 mm, 9 mm, etc. and 3 times according to the propagation of cracks during the loading process. When the bearing capacity of a specimen dropped to 85% of its ultimate load or the specimen failed, the loading process was terminated.

Every excursion in the inelastic range causes cumulative

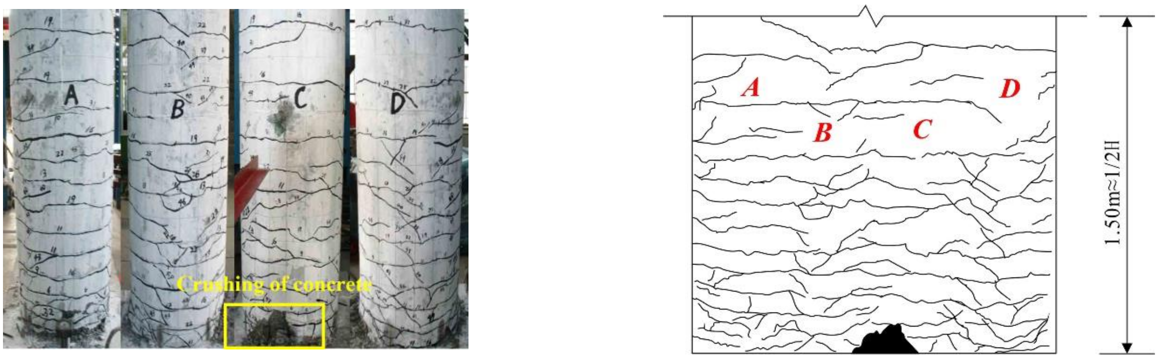

(a) TC-0.1

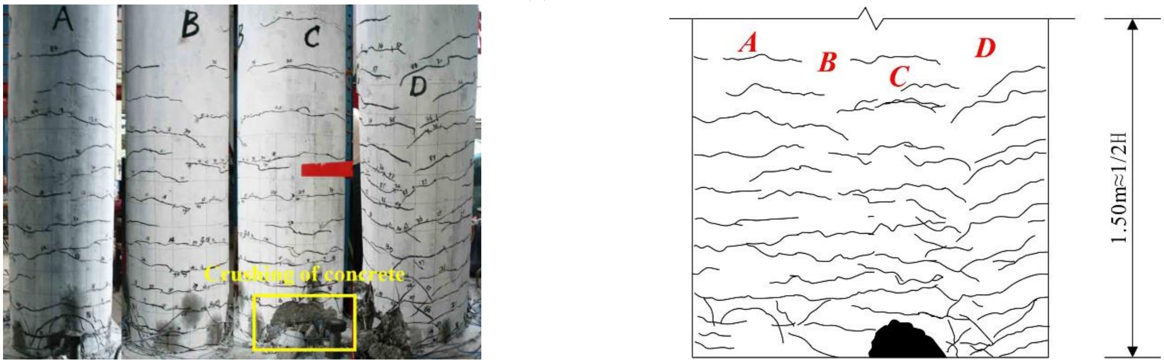

(b) TC-0.14

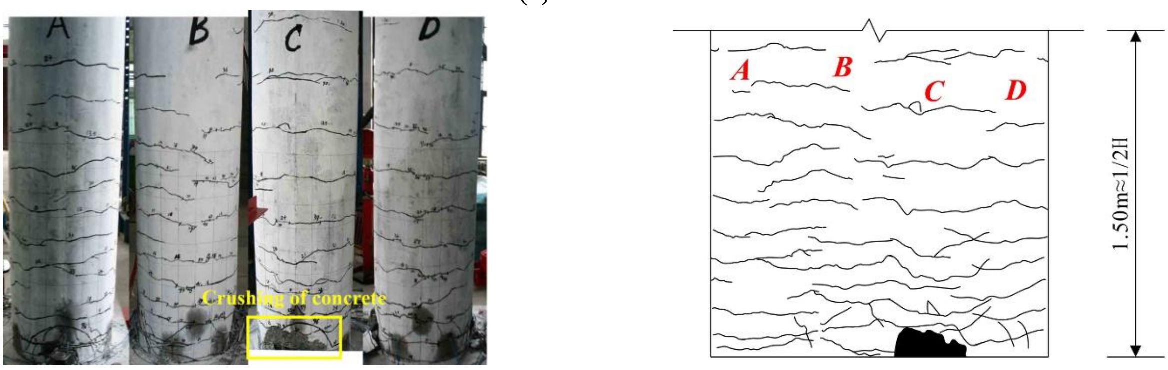

(c) TC-0.2

Fig. 6 Crack patterns of specimens

damage in the structural elements. In the adopted loading program, emphasis is given in the repetition of the inelastic excursions per loading step. The cycle number was 2 times after the occurrence of visible cracks, and changed to 3 times after the yielding of tensile longitudinal steel rebars. The increase of the cycle number in the inelastic range was applied for the complete propagation and development of cracks on the specimens. Meanwhile, the target displacement at each step was increased regularly. Cyclic loading tests adopted on three specimens all followed the above loading protocol. Figs. 5(b) - 5(d) present the practical loading sequences applied for three specimens during the tests.

2.2 Experimental results

2.2.1 Damage observation

Test results showed that the cracks mainly occurred on the lower half part of specimens during the cyclic loading test. Fig. 6 shows the crack patterns on the out-surface of specimens at the end of cyclic loading test. The four parts of out-surface (*A*, *B*, *C* and *D*) are indicated in Fig. 4. It can be observed that the horizontal cracks extended in the circumferential direction, and the diagonal cracks mainly occurred at the sides perpendicular to the loading direction (*B*-side and *D*-side). The crushing of concrete (shown in Fig. 6(d)) was observed at the bottom of *C*-side in all three specimens. Among three specimens, the specimen TC-0.1 presented the most cracks due to the minimum wall diameter ratio.

2.2.2 Strain analysis and failure mechanism

Fig. 7 shows the steel strains obtained from the strain gauges (Fig. 4) at the bottom of the specimens during the tests, including the strain variation of longitudinal steel rebars and the maximum strains of longitudinal steel rebars and stirrups. Where dashed lines are the yield strain of longitudinal steel rebars and stirrups listed in Table 2. It can

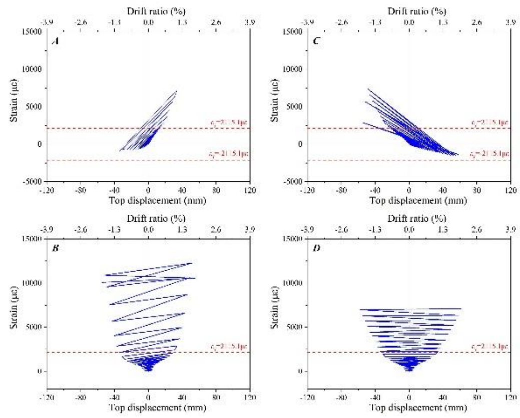

(a) Strains of longitudinal steel rebars in TC-0.1

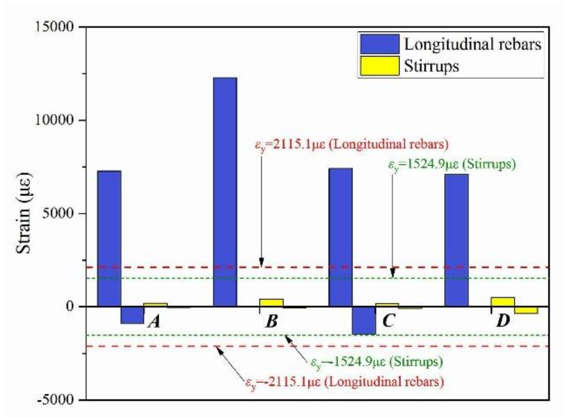

(b) Maximum steel strains in TC-0.1

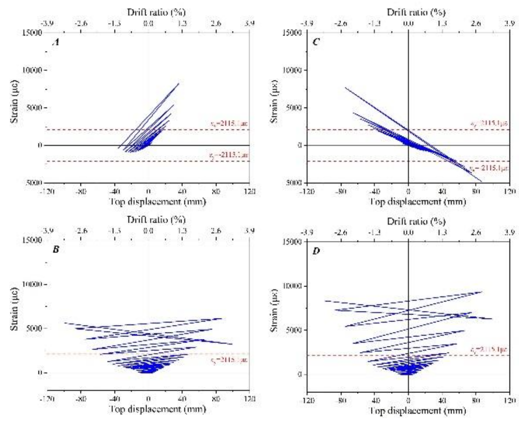

(c) Strains of longitudinal steel rebars in TC-0.14

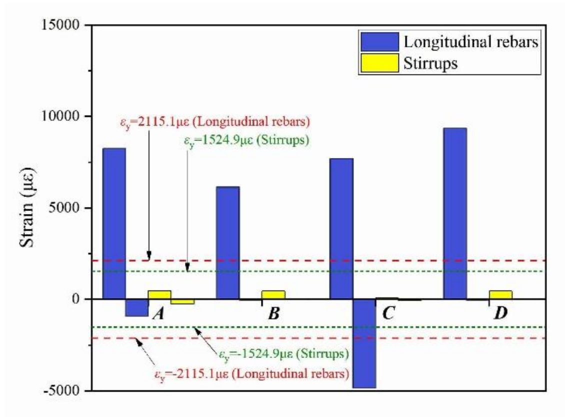

(d) Maximum steel strains in TC-0.14

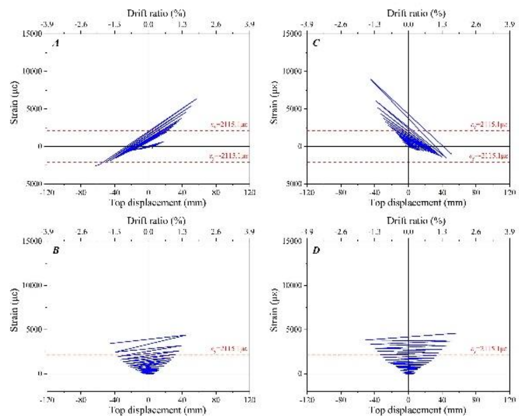

(e) Strains of longitudinal steel rebars in TC-0.2

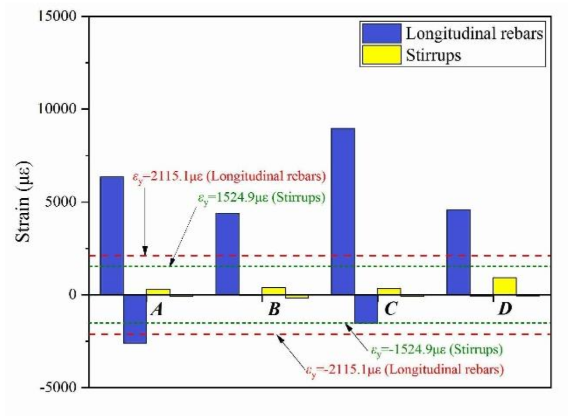

(f) Maximum steel strains in TC-0.2

Fig. 7 The strain of steels at the bottom of specimens

be found that longitudinal steel rebars at *A*-side and *C*-side of specimens were in the states of tension and compression alternately with the change of loading direction, while the longitudinal steel rebars at *B*-side and *D*-side were only tensioned throughout the whole loading process. That might because that *B*-side and *D*-side were in tensile regions after the concrete cracking, as a result of the migration of the neutral axis.

It can also be observed that the strains of longitudinal steel rebars in all tensile regions were larger than those in the compressive regions. And all the longitudinal steel rebars in tensile regions yielded, while most of longitudinal steel rebars in compressive regions did not yield. That was because the longitudinal steel rebars played a vital role in tensile regions to bear the tensile stress, while the stress in compressive regions was mostly borne by the concrete. In addition, it can be seen that the strains of stirrups at all four sides were far from the yield strain, showing sufficient shear resistance of RC tubular columns.

Moreover, so as to further investigate the stress status of longitudinal steel rebars, the lateral loading displacements corresponding to the first yielding of longitudinal steel rabars at four sides of specimens were summarized, and the yielding order of longitudinal steel rebars was also listed, as shown in Table 3. It should be noted that all longitudinal steel rebars at four sides exhibited tensile yielding. And the

Table 3 The applied lateral displacements corresponding to the first yielding of longitudinal steel rebars

Loading displacement (mm)	*A*-side	*B*-side	*C*-side	*D*-side	Yielding order of longitudinal steel rebars at four sides of specimen
TC-0.1	16.0	31.0	-22.0	34.0	*A*→*C*→*B*→*D*
TC-0.14	18.0	57.0	-42.0	48.0	*A*→*C*→*D*→*B*
TC-0.2	24.0	33.0	-18.0	-33.0	*C*→*A*→*B*→*D*

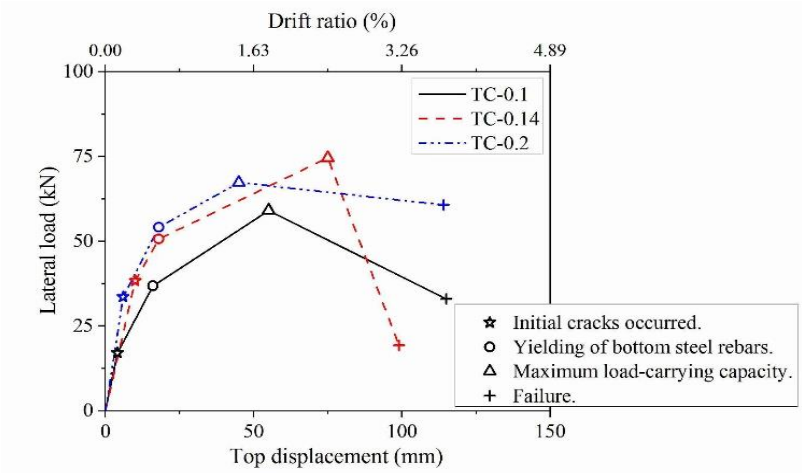

Fig. 8 Characteristic loading steps of specimens

longitudinal rebars at the sides along the loading direction (*A*-side and *C*-side) yielded first in all three specimens, then those at *B*-side and *D*-side yielded.

Based on the damage observations and strain analysis results, it can be concluded that all of the three specimens exhibited large bias compression failure modes, that is, the tensile longitudinal steel rebars yielded first while the compressive longitudinal steel rebars may not yield during the failure process, then the compressive concrete at the bottom of RC tubular column crushed with the buckling of longitudinal steel rebars.

2.2.3 Bearing capacity and characteristic loading steps

Fig. 8 shows the characteristic loading steps of specimens during the cyclic loading test corresponding to four damage states. The four damage states were defined as “initial cracks occurred”, “yielding of bottom tensile steel rebars”, “maximum load-carrying capacity” and “failure”, referring to Pagni and Lowes (2006). It can be found that TC-0.1 exhibited the earlier concrete cracking and longitudinal steel rebars yielding than the other specimens. This can be attributed to the small wall diameter ratio. The smaller the wall thickness (i.e., the concrete area), the sooner the concrete cracked. After the concrete cracking, the tensile stress was borne only by longitudinal steel rebars, resulting the earlier yielding of steel rebars.

Moreover, TC-0.14 presented the later initial cracking, the maximum bearing capacity, but the earlier failure among all specimens. This was owing to the large axial compression ratio. Although TC-0.2 had the largest wall diameter ratio, the crack resistance and the bearing capacity were restricted by the small axial compression ratio and longitudinal reinforcement ratio.

3. Numerical simulation approach and validation

3.1 General

In order to further investigate the seismic behavior of RC tubular columns under the effect of influence parameters, the FEA of numerical models was adopted based on the experimental study. The finite element models with fiber section for RC tubular columns were established through OpenSEES (McKenna and Fenves). Furthermore, the modeling approaches were validated through the comparative analysis between numerical and experimental results, to ensure the accuracy and availability of the numerical simulation for RC tubular columns.

As shown in Fig. 9(a), RC tubular columns without SDBs were simulated as a plane (two-dimensional) model. The influence parameters of seismic behaviors could be investigated by varying relevant setting parameters of the numerical models.

Among all the variable parameters, adding SDBs had a significant influence on the mechanical mechanism of RC tubular columns. Therefore, it is necessary to re-establish the numerical model for RC tubular columns with SDBs. Wang *et al*. (2018) found that the steel truss in novel air-cooled supporting structures is approximately on a plane motion under excitation. Accordingly, the steel truss could be simplified into a rigid plane. The three-dimensional model which has 6-degree-of-freedom nodes was applied to simulate RC tubular columns with SDBs, as shown in Fig. 9(b). The top node 3 is the main node. Nodes 6 - 11 are slave nodes whose degree-of-freedom in certain directions were constrained by Rigid Diaphragm Command. In addition, the SDBs were connected with columns directly instead of through the corbels, as a simplified modeling procedure.

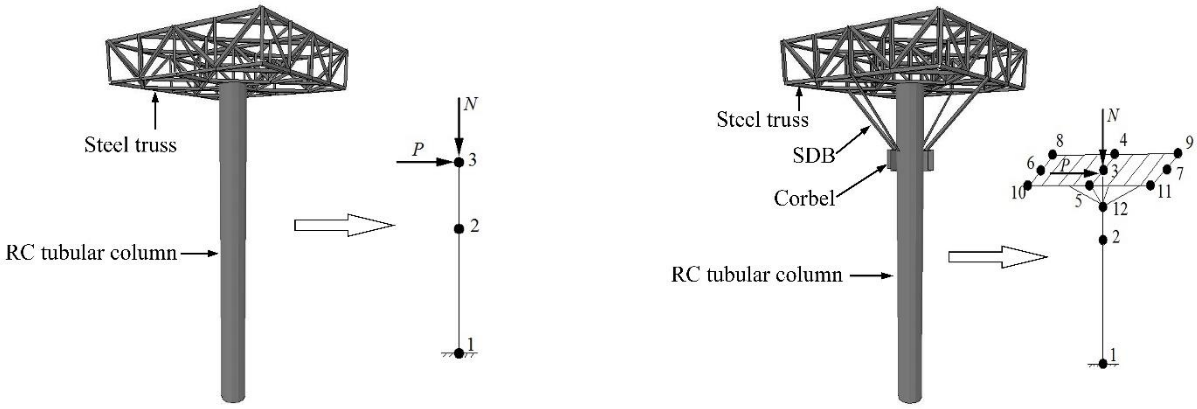

(a) Tubular column without SDBs (b) Tubular column with SDBs

Fig. 9 Simulation methods for RC tubular columns with and without SDBs

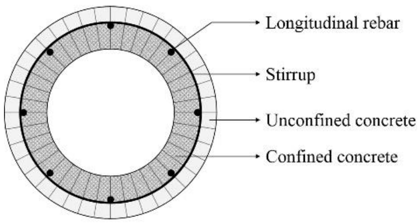

Fig. 10 Division of fiber section

3.2 Model of element

Nonlinear Beam-Column Element in OpenSEES was employed to simulate the RC tubular columns. P-Δ effect was taken into consideration owing to the large slenderness ratio of RC tubular columns. Five corresponding integration points were employed to calculate the stiffness and resistance. Considering the bond-slip behavior of steel rebars, the zero-length section element was inserted at the fixed bottom of column (Giuriani *et al*. 1991, Zhao and Sritharan 2007). The section of tubular column was divided into core area and cover area due to the confine of stirrups, as shown in Fig. 10.

For the RC tubular columns with SDBs, Nonlinear Beam-Column Element was selected to model the elements between slave nodes. And the SDBs were simulated as Truss Element, whose parameters should be consistent with measured material properties.

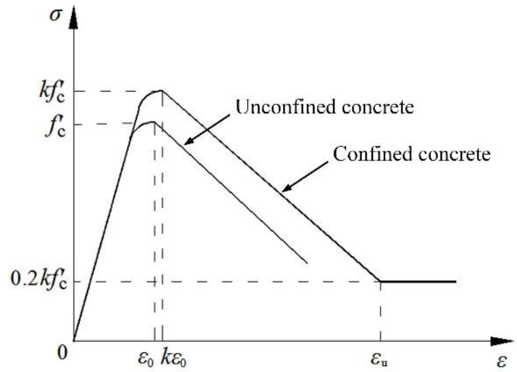

(a) Stress-strain skeleton curves of concrete

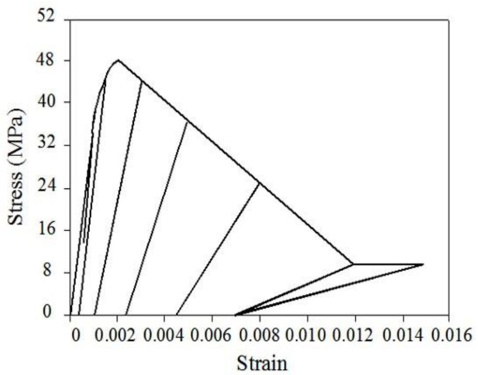

(b) Stress-strain hysteretic curves of concrete

Fig. 11 Concrete01 Material model in OpenSEES

3.3 Constitutive model of material

The stirrups in RC tubular columns were arranged with reasonable configuration and sufficient amount, providing appropriate constraint to the core concrete. The behavior of the core concrete exhibited different characteristics with the cover concrete. Therefore, the Concrete01 Material in OpenSEES was adopted to predict the behavior both of the core concrete and the cover concrete. Fig. 11 shows the constitutive relationships of this concrete material. This model is based on Kent-Scott-Park uniaxial stress-strain model (Kent 1969, Scott *et al*. 1982) with no tensile strength, considering the confinement effect of stirrup on ultimate strain, peak strength and ductility of the concrete.

As an important component of RC tubular columns, the steels (including longitudinal steel rebars and stirrps) has a significant influence on the seismic behavior of the whole structure. Hence, the model of steels directly effects the accuracy and validity of the structural numerical simulations. The Steel02 Material in OpenSEES (Menegotto and Pinto 1973, Filippou *et al*. 1983) was adopted to model the behavior of both longitudinal reinforcement and stirrups. This model is a uniaxial Giuffré-Menegotto-Pinto model taken isotropic hardening into account, exhibiting high computational efficiency and well simulation of the Bauschinger effect. Fig. 12 shows the stress-strain relationships of this steel model.

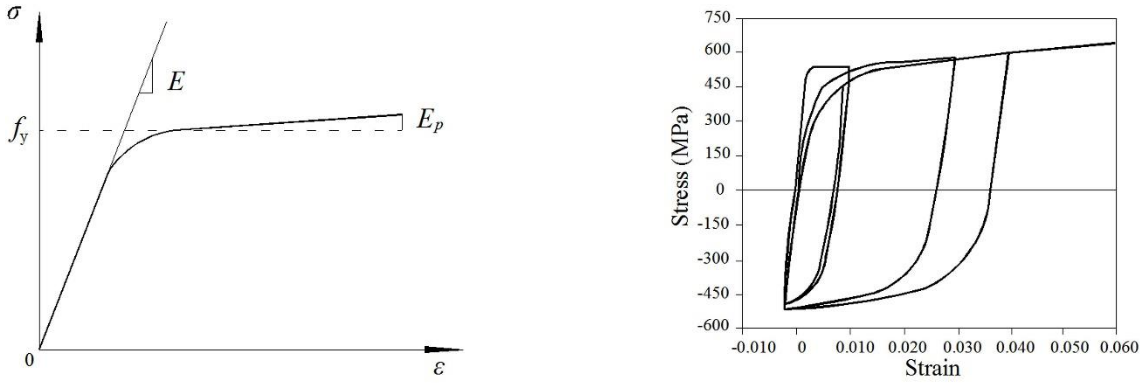

(a) Stress-strain skeleton curves of steel (b) Stress-strain hysteretic curves of steel

Fig. 12 Steel02 Material in OpenSEES

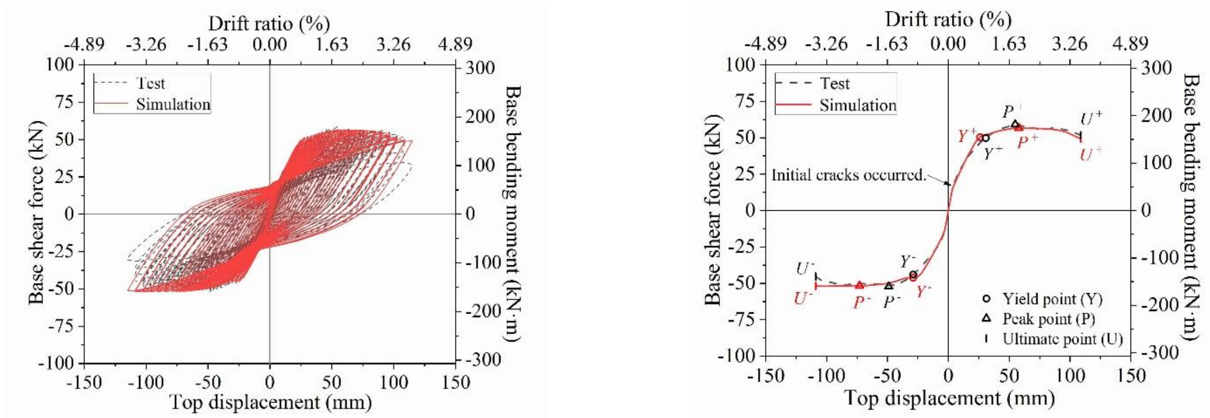

(a) Hysteretic curves (b) Skeleton curves

Fig. 13 Hysteretic and skeleton curves of specimen TC-0.1

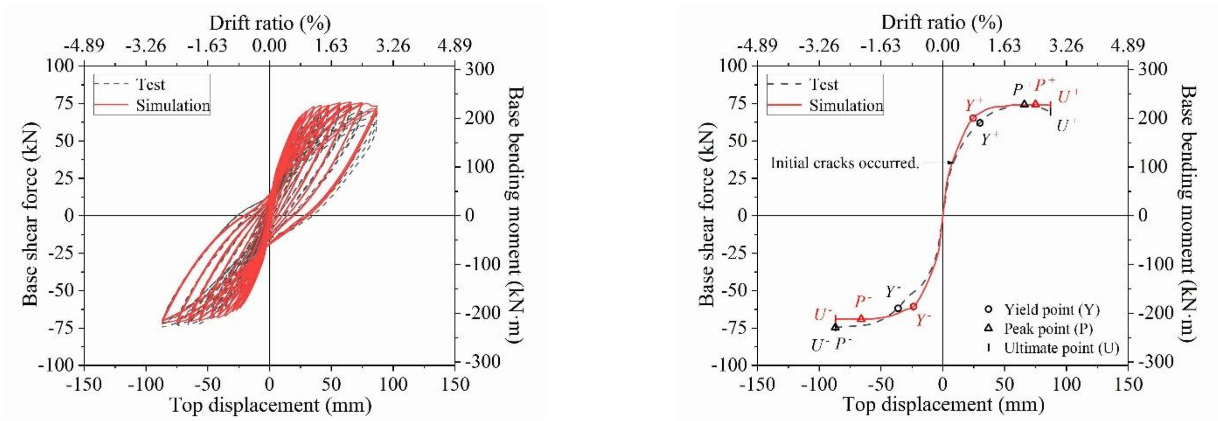

(a) Hysteretic curves (b) Skeleton curves

Fig. 14 Hysteretic and skeleton curves of specimen TC-0.14

3.4 Validation of numerical simulation method

Figs. 13 - 15 illustrate hysteretic and skeleton curves for base shear force versus top displacement of specimens obtained by cyclic loading tests and numerical simulation. The characteristic points designated on skeleton curves are listed in Table 4. The yield point was determined through the equivalent energy method (Park 1988), as shown in Fig. 16.

It can be observed that the numerical simulation results showed a good agreement with the test results in the shape of hysteretic curves, hysteretic loop area and characteristic points on skeleton curves. Both of the numerical and experimental skeleton curves consisted of the elasticity, elasto-plasticity, plasticity developing and softening phases. This indicated that the proposed finite element modeling approaches were reasonable to predict the seismic behavior of RC tubular columns.

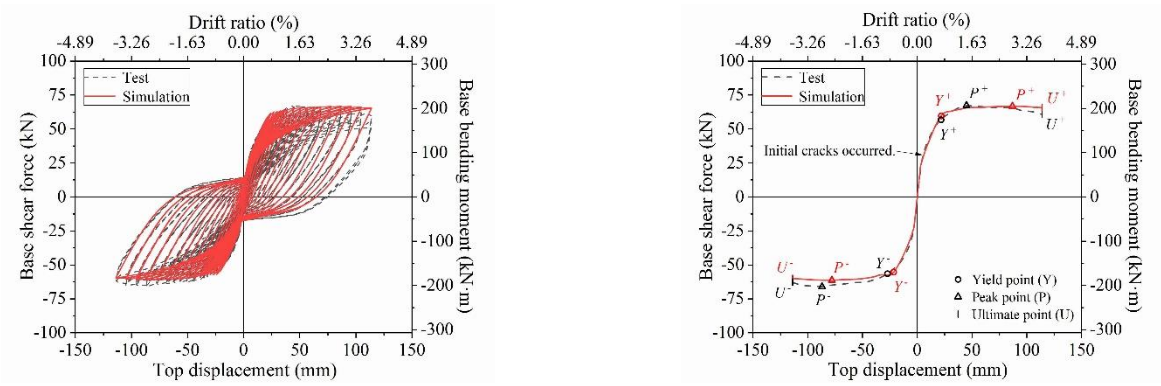

(a) Hysteretic curves (b) Skeleton curves

Fig. 15 Hysteretic and skeleton curves of specimen TC-0.2

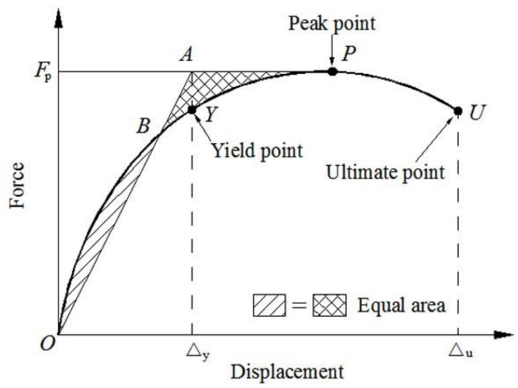

Fig. 16 Determination of the yield point through the equivalent energy method

Table 4 Characteristic points on skeleton curves

Specimen			Yield point		Peak point		Ultimate point	
			Disp. (mm)	Load (kN)	Disp. (mm)	Load (kN)	Disp. (mm)	Load (kN)
TC-0.1	Test	Positive	30.70	49.88	54.97	59.10	108.97	51.67
		Negative	-28.88	-43.91	-49.00	-52.18	-108.99	-45.31
	Simulation	Positive	26.03	50.39	58.02	56.68	109.02	49.23
		Negative	-28.98	-46.13	-72.98	-51.67	-108.98	-51.76
TC-0.14	Test	Positive	30.12	62.15	65.99	74.40	86.99	69.55
		Negative	-36.16	-61.78	-86.96	-74.58	-86.96	-74.58
	Simulation	Positive	24.57	65.30	75.03	74.50	87.03	73.84
		Negative	-23.69	-60.63	-65.97	-69.05	-86.97	-68.93
TC-0.2	Test	Positive	21.76	56.80	44.98	67.35	113.99	60.74
		Negative	-27.21	-56.49	-86.95	-66.08	-113.97	-62.91
	Simulation	Positive	21.98	59.71	87.01	66.76	114.01	65.73
		Negative	-21.55	-55.32	-77.99	-61.27	-113.99	-59.93

*Disp.: Displacement

Additionally, compared TC-0.14 with TC-0.1, it can be found that increasing the wall diameter ratio and axial compression ratio could lead to an increase in bearing capacity and a decrease in residual deformation and hysteretic loop area. And compared TC-0.2 with TC-0.1, bearing capacity and hysteretic loop area both increased as a result of the increase of wall diameter ratio and the decrease of longitudinal reinforcement ratio. Since the variable parameters in the tested specimens were coupled, and the influence law of parameters on the seismic behavior of RC tubular columns was uncertain. Therefore, it is necessary to conduct the independent study on each influence parameter.

4. Influence parameters of seismic behavior

4.1 Analysis method

The following sections present the parametric analysis

Table 5 The designed values of variable parameters in parametric analysis

Variable parameters	Designed values of variable parameters
Axial compression ratio ***n***	0.14; 0.27; 0.40
Longitudinal reinforcement ratio ***ρ***	1.00%; 1.66%; 2.44%
Stirrup reinforcement ratio $\boldsymbol{\rho_{sv}}$ (stirrup spacing)	0.68% (150mm); 1.01% (100mm); 2.05% (50mm)

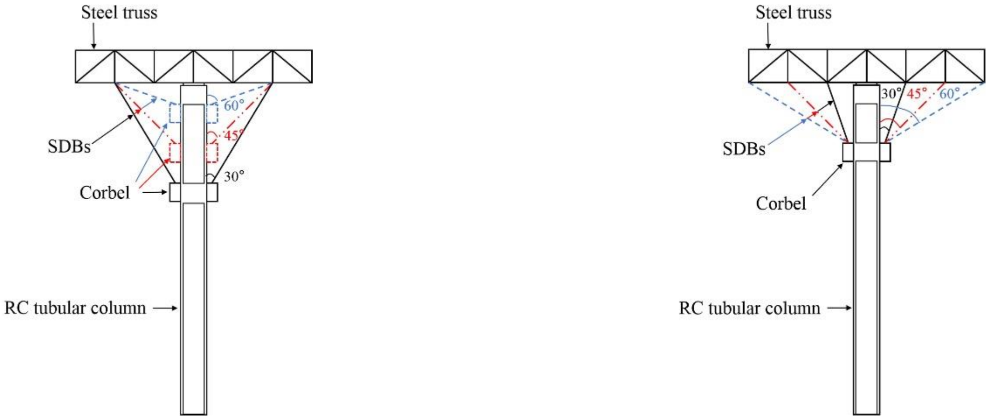

(a) With the same SDB-truss connecting position (b) With the same SDB-column connecting position

Fig. 17 Different setting positions and angles of SDBs

results based on the FEA of numerical models with variable parameters including axial compression ratio, longitudinal reinforcement ratio, stirrup reinforcement ratio and adding SDBs. Each variable parameter was investigated independently with three models, taking TC-0.1 as the standard specimen. The designed value of variable parameters are shown in Table 5. In addition, the mechanical and numerical analysis were conducted to reveal the influence of setting positions and angles of SDBs on seismic behavior of RC tubular columns, the setting details of SDBs are shown in Fig. 17.

The hysteretic behavior, bearing capacity, energy dissipation performance and lateral stiffness deterioration behavior of RC tubular columns were mainly compared based on the numerical analysis results to investigate the influence law of various parameters.

The cumulative hysteresis dissipated energy, calculated by the area enclosed by the force-displacement hysteretic loops, was employed to evaluate the accumulation of energy dissipation during the cyclic loading procedure. In addition, a useful indicator evaluating the energy dissipation capacity per loading cycle, the equivalent viscous damping coefficient ζ_{eq} (Karayannis and Golias 2018), was also adopted for comparing the energy dissipation capacity of RC tubular columns with different parameters. It can be derived from Fig. 18 and Eq. (1). The larger the equivalent viscous damping coefficient, the better the energy dissipation capacity.

$$\zeta_{eq} = \frac{1}{2\pi}\frac{S_{ABC} + S_{CDA}}{S_{OBE} + S_{ODF}} \tag{1}$$

Where, S_{ABC} and S_{CDA} are the upper and lower halves of the hysteretic loop area (S_{ABCD}) separated by the Displacement axis, respectively; S_{OBE} and S_{ODF} are the areas of triangles *OBE* and *ODF*, respectively. *O* is the origin of coordinates;

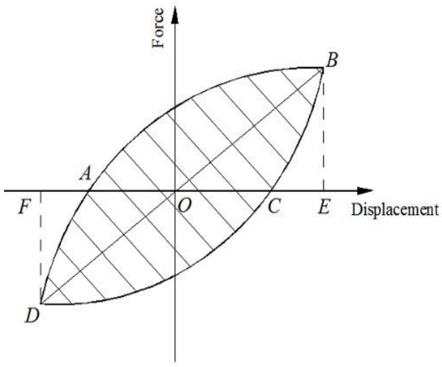

Fig. 18 Calculation diagram of equivalent viscous damping coefficient

E and *F* are the projection points on the Displacement axis corresponding to the hysteretic loop vertices *B* and *D*, respectively.

Besides, the lateral stiffness of RC tubular columns gradually deteriorated with the accumulation of damage, i.e., the cracks occurring and propagation. It can be calculated by Eq. (2).

$$K_i = \frac{|+P_i| + |-P_i|}{|+\Delta_i| + |-\Delta_i|} \tag{2}$$

Where, $+\Delta_i$ and $-\Delta_i$ are respectively the applied displacement amplitude of the *i*-th cyclic loading case of the cyclic loading tests in two opposite directions; $+P_i$ and $-P_i$ are respectively the load corresponding to $+\Delta_i$ and $-\Delta_i$.

4.2 Axial compression ratio

Figs. 19(a) and 19(b) show the hysteretic and skeleton

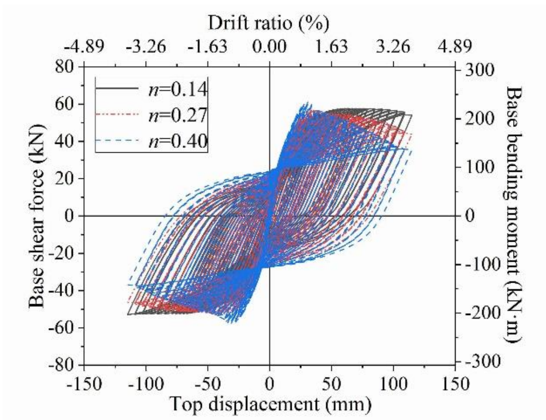

(a) Hysteretic curves

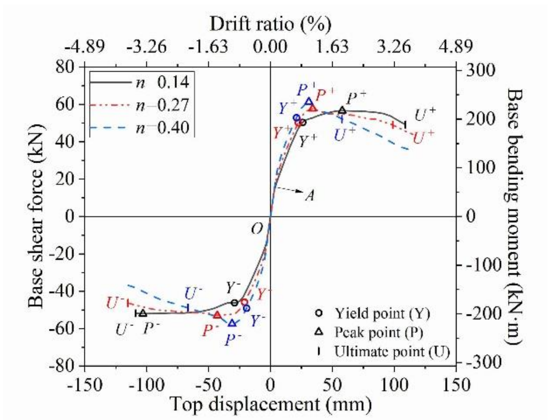

(b) Skeleton curves

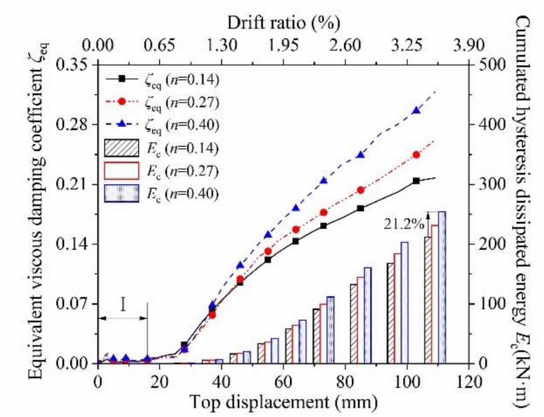

(c) Equivalent viscous damping coefficient and cumulative hysteresis dissipated energy

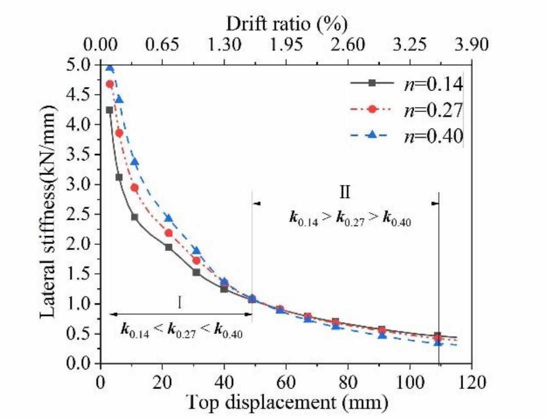

(d) Stiffness deterioration curves

Fig. 19 Hysteretic behaviors under different axial compression ratios

Table 6 Characteristic points under different axial compression ratios

Axial compression ratio	n=0.14		n=0.27		n=0.40	
	Positive	Negative	Positive	Negative	Positive	Negative
Yield Displacement (mm)	26.03	-28.98	22.51	-20.94	21.04	-19.28
Yield Load (kN)	50.39	-46.13	50.19	-45.76	52.91	-49.03
Peak Displacement (mm)	58.02	-102.98	34.05	-42.95	31.05	-30.95
Peak Load (kN)	56.68	-51.96	57.74	-52.93	61.40	-57.39
Ultimate Displacement (mm)	109.02	-108.98	98.77	-114.95	57.87	-66.69
Ultimate Load (kN)	49.23	-51.76	49.08	-46.27	52.20	-48.81

curves for base shear force versus top displacement corresponding to different axial compression ratios. Characteristic points designated on skeleton curves are listed in Table 6. It can be found that the bearing capacity was enhanced with increase of the axial compression ratio, while the descending branch of the specimen with larger axial compression ratio became to be steeper, indicating that increasing the axial compression ratio would weaken the ductility.

As the axial compression ratio increased, the depth of compression region on cross section increased, while the tensile stress of longitudinal steel rebars decreased. Therefore, the yielding of longitudinal steel rebars required a larger lateral load, resulting the enhancement of the bearing capacity. And the concrete in compression regions would crushed before the yielding of tensile longitudinal steel rebars, which could accounted for the weaker ductility as the increase of axial compression ratio.

Fig. 19(c) shows the calculated equivalent viscous damping coefficients and the cumulative hysteresis dissipated energy under different axial compression ratios. It can be observed that the equivalent viscous damping coefficient had nearly no change in the first stage, then it increased quickly due to the occurrence and propagation of cracks. Especially, when the loading displacement was larger than 40 mm, the equivalent viscous damping coefficient of RC tubular column with larger axial compression ratio had a significant larger value than that with lower axial compression ratio. It can also be found that the cumulative hysteresis dissipated energy gradually increased with the increase of applied displacement, as a result of damage accumulation and plastic development.

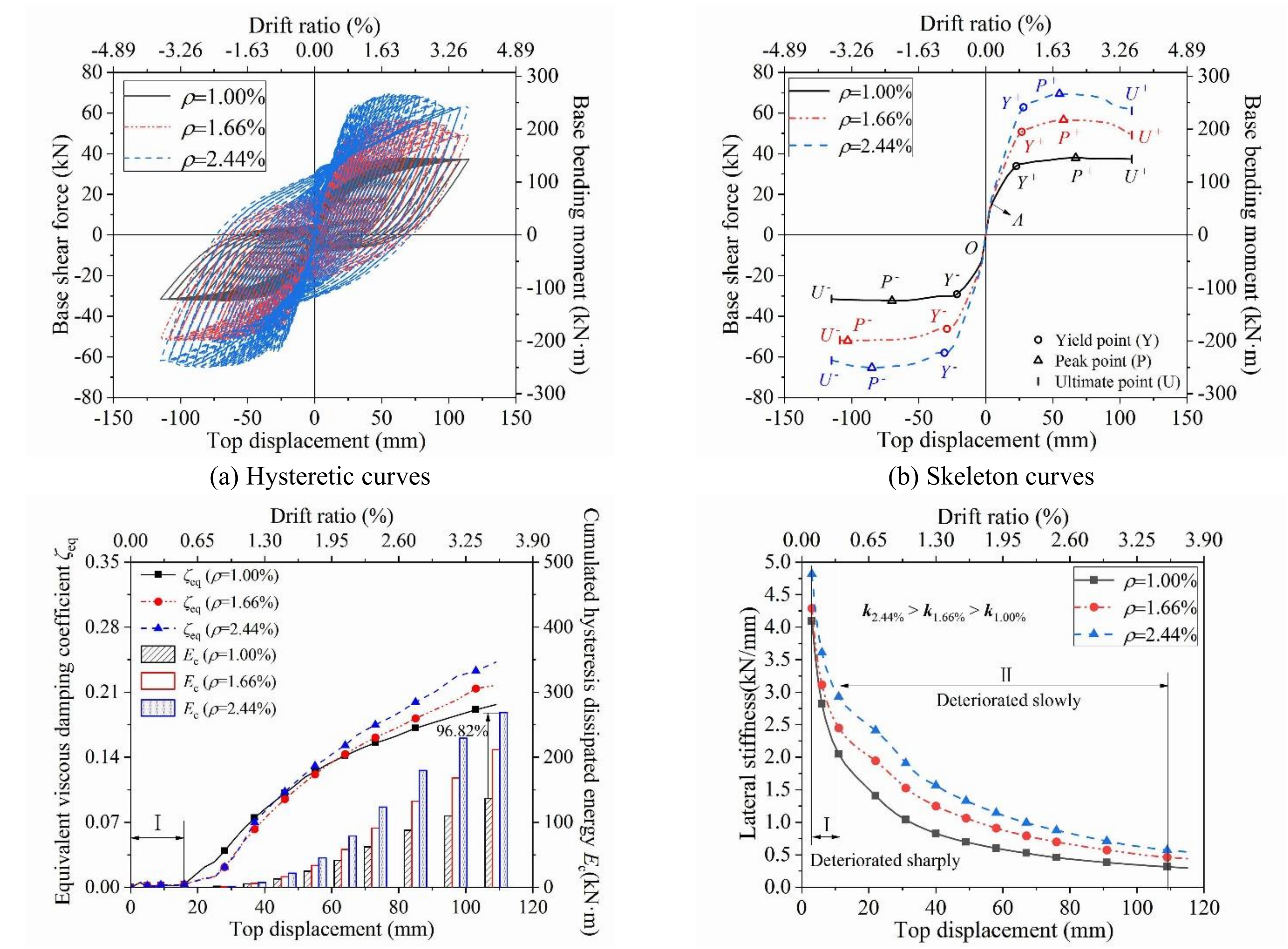

(a) Hysteretic curves

(b) Skeleton curves

(c) Equivalent viscous damping coefficient and cumulative hysteresis dissipated energy

(d) Stiffness deterioration curves

Fig. 20 Hysteretic behaviors under different longitudinal reinforcement ratios

Table 7 Characteristic points under different longitudinal reinforcement ratios

Longitudinal reinforcement ratio	ρ=1.00%		ρ=1.66%		ρ=2.44%	
	Positive	Negative	Positive	Negative	Positive	Negative
Yield Displacement (mm)	22.71	-21.61	26.03	-28.98	28.14	-30.90
Yield Load (kN)	33.99	-29.12	50.39	-46.13	62.93	-57.95
Peak Displacement (mm)	67.02	-69.98	58.02	-102.98	55.02	-84.98
Peak Load (kN)	38.00	-32.38	56.68	-51.96	69.49	-65.28
Ultimate Displacement (mm)	109.02	-114.98	109.02	-108.98	109.02	-114.98
Ultimate Load (kN)	37.40	-31.52	49.23	-51.76	61.11	-61.74

When the axial compression ratio changed from 0.14 to 0.4, the cumulative hysteresis dissipated energy was enhanced by around 20.4%. These indicated that the increase of axial compression ratio was favorable to the energy dissipation capacity of RC tubular columns.

Fig. 19(d) shows the lateral stiffness deterioration curves under different axial compression ratios. It can be found that the initial lateral stiffness increased with the increase of the axial compression ratio, while the speed of stiffness deterioration also increased. At the later loading stage, RC tubular columns with larger axial compression ratio had a smaller lateral stiffness than those with smaller axial compression ratio.

4.3 Longitudinal reinforcement ratio

Figs. 20(a) and 20(b) show the hysteretic and skeleton force-displacement curves corresponding to different longitudinal reinforcement ratios. Characteristic points designated on skeleton curves are listed in Table 7. It can be seen that the longitudinal reinforcement ratio had a large positively correlated impact on the hysteretic behavior of RC tubular columns. As shown in Fig. 20(a), increasing the longitudinal reinforcement ratio led to an increase in hysteretic loop area and a reduction in pinching effect. It is obvious in Fig. 20(b) that the skeleton curves were divided into elastic (line-*OA*), hardening (line-*AP*) and softening (line-*PU*) phases by characteristic points. The bearing

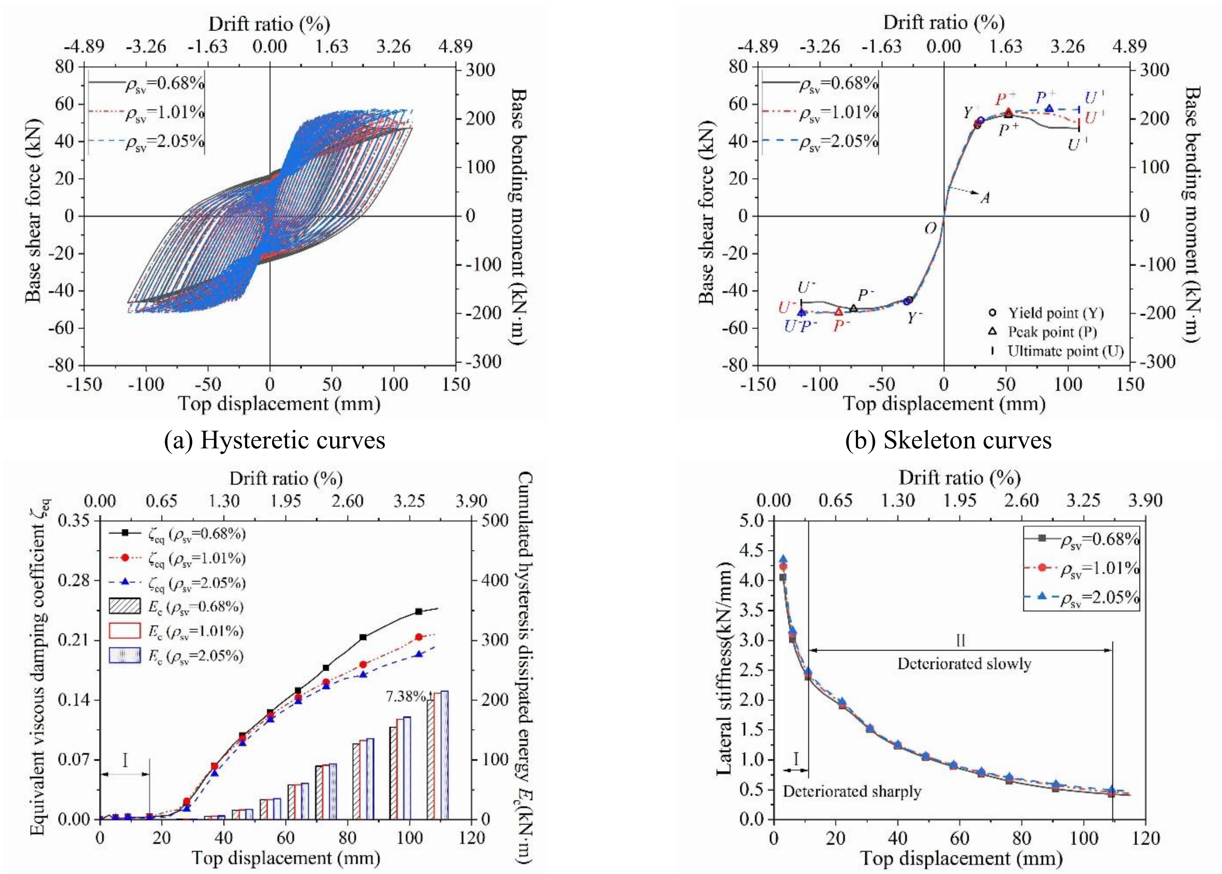

(a) Hysteretic curves

(b) Skeleton curves

(c) Equivalent viscous damping coefficient and cumulative hysteresis dissipated energy

(d) Stiffness deterioration curves

Fig. 21 Hysteretic behaviors under different stirrup reinforcement ratios

Table 8 Characteristic points under different stirrup reinforcement ratios

Stirrup reinforcement ratio	ρ_{sv}=0.68%		ρ_{sv}=1.01%		ρ_{sv}=2.05%	
	Positive	Negative	Positive	Negative	Positive	Negative
Yield Displacement (mm)	26.86	-27.82	27.36	-29.84	29.67	-30.12
Yield Load (kN)	48.74	-44.67	50.03	-45.57	51.44	-45.75
Peak Displacement (mm)	52.02	-72.98	52.02	-84.98	85.02	-114.98
Peak Load (kN)	54.26	-49.60	55.71	-51.57	57.39	-51.79
Ultimate Displacement (mm)	109.02	-114.98	109.02	-114.98	109.02	-114.98
Ultimate Load (kN)	47.15	-46.32	50.53	-50.70	57.17	-51.79

capacity provided an extraordinary enhancement of around 82.9% when longitudinal reinforcement ratio increased from 1.00% to 2.44%.

Fig. 20(c) shows the calculated equivalent viscous damping coefficients and the cumulative hysteresis dissipated energy under different longitudinal reinforcement ratio. It can be observed that the equivalent viscous damping coefficients of RC tubular columns provided an increase with the increase of longitudinal reinforcement ratio, especially when the loading displacement was larger than 60 mm. And the cumulative hysteresis dissipated energy had a remarkable growth of around 96.8% when the longitudinal reinforcement ratio increased from 1.00% to 2.44%.

There was an improvement of both lateral bearing capacity and energy dissipation capacity with the increase of longitudinal reinforcement ratio. After concrete cracking in tension region, due to the increase of steel rebars tension strain and the migration of neutral axis, the stress states of partial longitudinal steel rebars were changed from compression to tension. Accordingly, the increase of longitudinal reinforcement ratio was actually the increase of tensile longitudinal steel rebars, which enhanced the tensile behavior of RC tubular columns after the concrete cracking.

Fig. 20(d) shows the lateral stiffness deterioration curves under different longitudinal reinforcement ratios. It can be seen that the longitudinal reinforcement ratio had a significant effect on lateral stiffness deterioration. The larger the longitudinal reinforcement ratio, the larger the lateral stiffness. Moreover, it can be found that the lateral stiffness deteriorated sharply in the first stage due to the concrete cracking. Then, it deteriorated slowly in the second stage, this might be caused by the accumulated damage with the increase of applied displacement.

4.4 Stirrup reinforcement ratio

Figs. 21(a) and 21(b) show the hysteretic and skeleton force-displacement curves corresponding to different stirrup reinforcement ratios. Characteristic points designated on skeleton curves are listed in Table 8. As shown in Fig. 21(b), the stirrup reinforcement ratio had almost no influence on the skeleton curves before the yield point. After that, the softening segment, i.e. the strength deterioration, was moderated with the increase of stirrup reinforcement ratio, indicating that increasing the stirrup reinforcement ratio was favorable to the ductility.

Fig. 21(c) shows the calculated equivalent viscous damping coefficients and the cumulative hysteresis dissipated energy under different longitudinal reinforcement ratio. It could be observed that there was a reduction of equivalent viscous damping coefficient at later loading stage as increasing the stirrup reinforcement ratio. And the cumulative hysteresis dissipated energy curves had little change varying the stirrup reinforcement ratio. That might be attributable to the thin wall thickness and the limited confined concrete region of RC tubular columns.

Fig. 21(d) shows the lateral stiffness deterioration curves under different stirrup reinforcement ratios. It can be observed that the stirrup reinforcement ratio had a little influence on lateral stiffness. In the first stage, the curves showed an almost linear descending owing to the cracks occurrence. Then, the lateral stiffness deteriorated slowly with the increase of applied displacement in the second stage, caused by the damage cumulation.

As shown above, the stirrup reinforcement ratio had little effect on the seismic behavior of RC tubular columns, including bearing capacity, energy dissipation capacity and stiffness deterioration. In fact, the confinement effect of stirrups in hollow section columns is different from that in solid columns. In the hollow column section, the confined concrete could move toward the section center because of the hole. While in the solid section, the core confined concrete is under compression in three directions. As the hole size increases, the effect of stirrup confinement is smaller (Lignola *et al.* 2008). Moreover, transverse reinforcement configuration of two layers stirrups with cross ties provides stronger confinement effect on the concrete than a single layer stirrups (Xiao and Sritharan 2018). Therefore, with the wall diameter ratio of 0.1, stirrups had small restriction on the concrete in RC tubular columns of air-cooled supporting structures. Furthermore, a single layer of stirrups were arranged in the specimens and numerical models, providing less confinement effect on the concrete than two layers stirrups with cross ties in the prototype.

4.5 Adding SDBs

Fig. 22 shows the hysteretic and skeleton force-displacement curves of RC tubular columns with the same SDB-truss connecting position. Characteristic points designated on skeleton curves are listed in Table 9. It can be observed that the columns with SDBs exhibited a larger initial slope of skeleton curves than those without SDBs, as well as a larger hysteretic loop area and peak load, indicating that adding SDBs could enhance the lateral stiffness, energy dissipation capacity and bearing capacity of RC tubular columns.

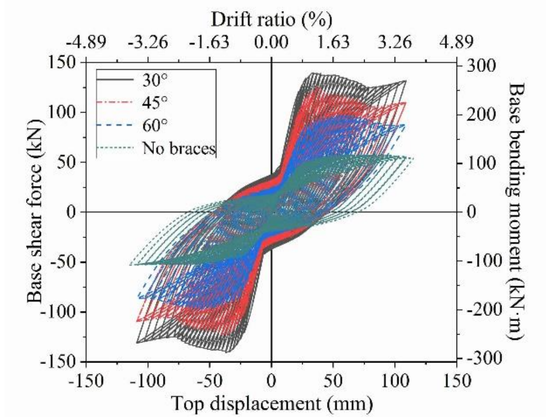

(a) Hysteretic curves

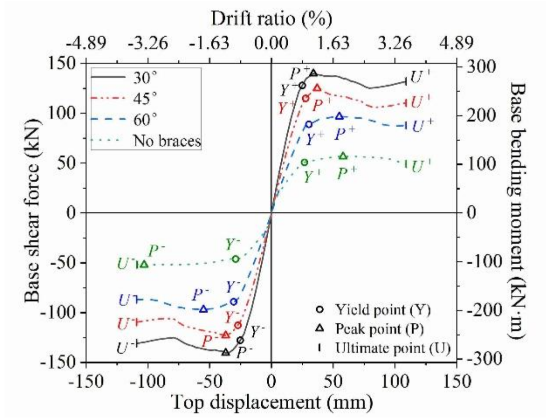

(b) Skeleton curves

Fig. 22 Hysteretic and skeleton curves of RC tubular columns with the same SDB-truss connecting position

Moreover, it can be found that decreasing the setting angle was beneficial to the seismic behavior for RC tubular columns with the same SDB-truss connecting position. The lateral stiffness, energy dissipation capacity and bearing capacity were all enhanced with the decrease of the setting angle.

Fig. 23 shows the hysteretic and skeleton force-displacement curves of RC tubular columns with the same SDB-column connecting position. Characteristic points designated on skeleton curves are listed in Table 10. It can be observed that the SDBs setting angle had little influence on the seismic behavior for RC tubular columns with the same SDB-column connecting position.

Figs. 24 - 25 present the load transfer paths and the bending moment distribution patterns of RC tubular columns with and without SDBs subjected to the lateral force. It can be found that the load transfer paths from steel truss to the upper column changed after adding the SDBs. As shown in Fig. 24, all the forces were directly transferred to column through the truss-to-column joint for RC tubular columns without SDBs. Nevertheless, for RC tubular columns with SDBs, except the forces directly transferred

Table 9 Characteristic points of tubular columns with the same SDB-truss connecting position

Setting angle of SDBs	30°		45°		60°		No braces	
	Positive	Negative	Positive	Negative	Positive	Negative	Positive	Negative
Yield Displacement (mm)	26.05	-26.19	27.73	-27.17	30.68	-30.02	26.76	-28.98
Yield Load (kN)	105.22	-103.66	115.14	-112.55	103.53	-101.32	50.83	-46.13
Peak Displacement (mm)	46.00	-46.00	37.00	-37.00	43.00	-43.00	58.02	-102.98
Peak Load (kN)	114.54	-114.31	125.14	-122.83	112.76	-110.61	56.68	-51.96
Ultimate Displacement (mm)	109.00	-109.00	109.00	-109.00	109.00	-109.00	109.02	-108.98
Ultimate Load (kN)	110.93	-109.79	110.41	-109.42	98.54	-97.44	49.23	-51.76

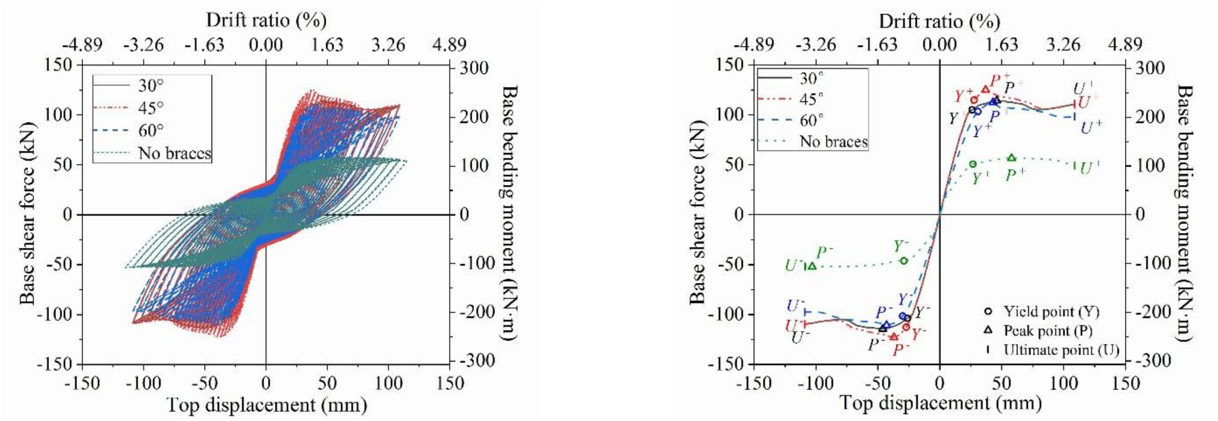

(a) Hysteretic curves (b) Skeleton curves

Fig. 23 Hysteretic and skeleton curves of RC tubular columns with the same SDB-column connecting position

Table 10 Characteristic points of tubular columns with the same SDB-column connecting position

Setting angle of SDBs	30°		45°		60°		No braces	
	Positive	Negative	Positive	Negative	Positive	Negative	Positive	Negative
Yield Displacement (mm)	26.05	-26.19	27.73	-27.17	30.68	-30.02	26.76	-28.98
Yield Load (kN)	105.22	-103.66	115.14	-112.55	103.53	-101.32	50.83	-46.13
Peak Displacement (mm)	46.00	-46.00	37.00	-37.00	43.00	-43.00	58.02	-102.98
Peak Load (kN)	114.54	-114.31	125.14	-122.83	112.76	-110.61	56.68	-51.96
Ultimate Displacement (mm)	109.00	-109.00	109.00	-109.00	109.00	-109.00	109.02	-108.98
Ultimate Load (kN)	110.93	-109.79	110.41	-109.42	98.54	-97.44	49.23	-51.76

to the column, part of the forces could be transferred through SDBs, as shown in Fig. 25. This can explain why the bearing capacity of RC tubular columns with SDBs was larger than that without SDBs.

For RC tubular columns with the same SDB-truss connecting position, with the decrease of setting angle, the position of corbels moved down, as shown in Fig. 17(a). Correspondingly, the position of inflection point for the RC tubular column moved down (see Fig. 25), and the bending moment distributed at the bottom of column (M_b) decreased. Therefore, the failure of tubular column required a larger lateral force, which means that the bearing capacity of tubular column could be enhanced with the decrease of the setting angle. However, for RC tubular columns with the same SDB-column connecting position, varying the SDBs setting angle nearly has no change in the position of corbel and inflection point, indicating that the SDB-truss connecting position nearly has no influence on the seismic behavior of RC tubular columns.

5. Conclusions

In this paper, the seismic behavior and its influence parameters of large-scale thin-walled RC tubular columns in air-cooled supporting structure of TPPs were investigated through experimental and numerical analysis. The following conclusions can be drawn:

- The cracks mainly occurred on the lower half part of specimens during the cyclic loading test. The specimen with the minimum wall diameter ratio presented the earlier cracking and the most cracks on the out-surface. The failure model is large bias compression failure induced by the concrete crushing at the bottom of columns.
- The numerical simulation results exhibited a good agreement with experimental results, indicating that the proposed finite element modeling approaches are reasonable to predict the seismic behavior of thin-walled

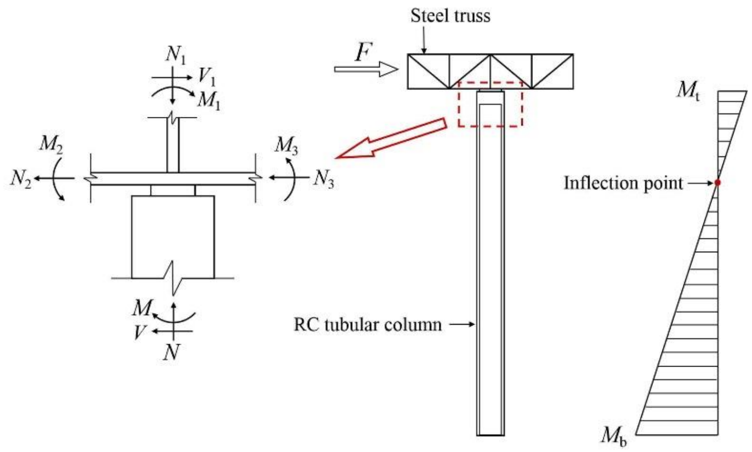

Fig. 24 Mechanical analysis of RC tubular columns without SDBs

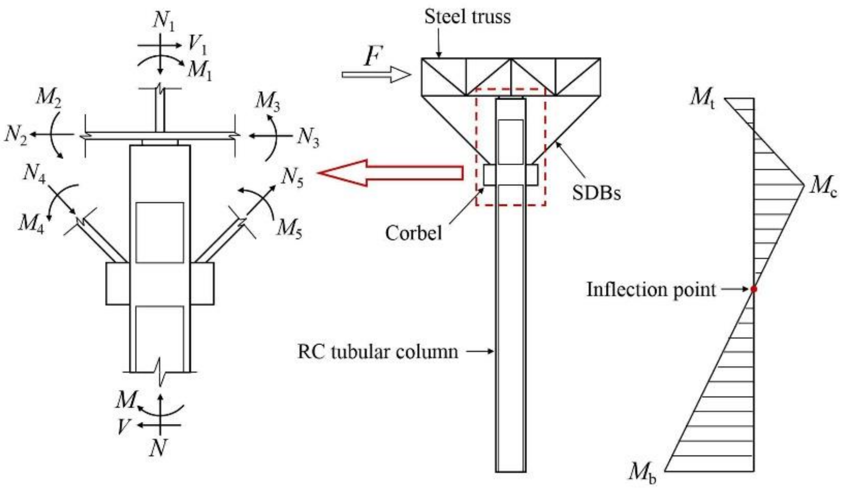

Fig. 25 Mechanical analysis of RC tubular columns with SDBs

RC tubular columns in air-cooled supporting structures of TPPs.

• The axial compression ratio shows a great effect on the seismic behavior of RC tubular columns. Increasing the axial compression ratio could lead to the increase of lateral bearing capacity and energy dissipation capacity, but also aggravate both of strength and lateral stiffness deterioration after the peak point, i.e. weaken the ductility. This could be attributed to the increase of compression region depth on cross section.

• The longitudinal reinforcement ratio has a significant influence on the seismic behavior of RC tubular columns. Increasing the longitudinal reinforcement ratio could effectively enhance the lateral stiffness, bearing capacity and energy dissipation capacity. This is caused by the enhancement of tensile behavior of RC tubular columns after the concrete cracking.

• Due to the thin wall thickness and the limited confined concrete region, the stirrup reinforcement ratio slightly affects the seismic behavior of RC tubular columns. The strength deterioration after the peak point is moderated with the increase of stirrup reinforcement ratio, indicating that increasing the stirrup reinforcement ratio is favorable to the ductility.

• Adding SDBs exhibits extraordinary effects on the seismic behavior of RC tubular columns. RC tubular columns with SDBs have a much higher bearing capacity and lateral stiffness than those without SDBs. That is because part of forces could be transferred through SDBs, except the forces directly transferred to the column. The SDB-column connecting position has a great impact on seismic behavior of RC tubular columns, while the SDB-truss connecting position nearly has no influence on the seismic behavior. And decreasing the angle between columns and SDBs could significantly enhance the lateral stiffness, bearing capacity and energy dissipation capacity.

Acknowledgments

This work was supported by the National Natural Science Foundation of China (NSFC, Grant No. 51708037 and 51978076), the Natural Science Foundation of Shaanxi Province (Grant No. 2019JQ-193) and the Fundamental

Research Funds for the Central Universities, CHD (Grant No. 300102280202). In addition, special thanks to chief engineer Dr. Hongxing Li from Northwest Electronic Power Design Institute for helpful and valuable discussions on the experimental analysis

References

Bustamante, J.G., Rattner, A.S., Garimella, S. (2015), "Achieving near-water-cooled power plant performance with air-cooled condensers", *Appl. Therm. Eng*., **72**, 1-10. http://dx.doi.org/10.1016/j.applthermaleng.2015.05.065.

Filippou, F.C., Popov, E.P. and Bertero, V.V. (1983), "Effects of Bond Deterioration on Hysteretic Behavior of Reinforced Concrete Joints", Report No. EERC 83-19; Earthquake Engineering Research Center, University of California, Berkeley.

Giuriani, E., Plizzari, G. and Schumm, C. (1991), "Role of stirrups and residual tensile strength of cracked concrete on bond", *J. Struct. Eng*., **117**(1), 1-18. http://dx.doi.org/10.1061/(ASCE)0733-9445(1991)117:1(1).

Han, Q., Zhou, Y.L., Du, X.L., Huang, C. and Lee, G.C. (2014), "Experimental and numerical studies on seismic performance of hollow RC bridge columns", *Earthq. Struct*., **7**(3), 251-269. http://dx.doi.org/10.12989/eas.2014.7.3.251.

Jiang, L.Y., Chu, J.X. and Cao, Y.S. (2011), "Static and dynamic analysis of the air-cooled condenser platform structure in thermal power plant", *Advan. Mat. Res*., **374-377**, 480-483. http://dx.doi.org/10.4028/www.scientific.net/AMR.374-377.480.

Kakaletsis, D.J., David, K.N. and Karayannis, C.G. (2011), "Effectiveness of some conventional seismic retrofitting techniques for bare and infilled R/C frames", *Struct. Eng. Mech*., **39**(4), 499-520. https://doi.org/10.12989/sem.2011.39.4.499.

Karayannis, C.G. and Golias, E. (2018), "Full scale tests of RC joints with minor to moderate seismic damage repaired using C-FRP sheets", *Earthq. Struct*., **15**(6), 617-627. https://doi.org/10.12989/eas.2018.15.6.617.

Kent, D.C. (1969), "Inelastic Behavior of Reinforced Concrete Members with Cyclic Loading", University of Canterbury, Christchurch, New Zealand.

Lee, J.H., Choi, J.H., Hwang, D.K. and Kwahk, I.J. (2015), "Seismic performance of circular hollow RC bridge columns", *KSCE J. Civil Eng*., **19**(5), 1456-1467. http://dx.doi.org/10.1007/s12205-014-1173-z.

Lignola, G.P., Prota, A., Manfredi, G. and Cosenza, E. (2008), "Unified theory for confinement of rc solid and hollow circular columns", *Compos. Part B* (*Eng.*), **39**(7-8), 1151-1160. http://dx.doi.org/10.1016/j.compositesb.2008.03.007.

McKenna, F. and Fenves, G.L. "The OpenSEES Command Language Primer", PEER, University of California, Berkeley, USA. http://opensees. berkeley. edu.

Menegotto, M. and Pinto, P.E. (1973), "Method of analysis for cyclically loaded RC plane frames including changes in geometry and non-elastic behavior of elements under combined normal force and bending", *In the Proceedings of IABSE Symposium on Resistance and Ultimate Deformability of Structures.* International Association for Bridge and Structural Engineering, Lisbon.

Mokrin, Z.A.R. (1988), "Energy evaluation in reinforced concrete hollow circular sections under bending", *Eng. Struct*., **10**(4), 281-286. http://dx.doi.org/10.1016/0141-0296(88)90050-8.

Odabaee, M., Hooman, K. (2011), "Application of metal foams in air-cooled condensers for geothermal power plants: An optimization study", *Int. Commu. Heat Mass,* **38**, 838-843. http://dx.doi.org/10.1016/j.icheatmasstransfer.2011.03.028.

O'Donovan, A., Grimes, R. (2014), "A theoretical and experimental investigation into the thermodynamic performance of a 50 MW power plant with a novel modular air-cooled condenser", *Appl. Therm. Eng*., **71**, 119-129. http://dx.doi.org/10.1016/j.applthermaleng.2014.06.045.

Pagni, C.A. and Lowes, L.N. (2006), "Fragility functions for older reinforced concrete beam-column joints", *Earthq. Spectra*, **22**(1), 215-238. https://doi.org/10.1193/1.2163365.

Park, R. (1988), "State of the art report ductility evaluation from laboratory and analytical testing", *In the Proceedings of Ninth World Conference on Earthquake Engineering*, Tokyo.

Scott, H.D., Park, R. and Priestly, M.J.N. (1982), "Stress-strain behavior of concrete confined by overlapping hoops at low and high strain rates", *J. Amer. Concrete Institute*, **79**(1), 13-27.

Tayem, A. and Najmi, A. (1996), "Design of round reinforced-concrete columns", *J. Struct. Eng*., **122**(9), 1062-1071. http://dx.doi.org/10.1061/(ASCE)0733-9445(1996)122:9(1062).

Tsonos, A.G. (2007), "Cyclic load behavior of reinforced concrete beam-column subassemblages of modern structures", *ACI Struct. J*., **104**(4), 468-478. https://doi.org/10.14359/18777.

Tsonos, A.G. (2014), "An innovative solution for strengthening of old R/C structures and for improving the FRP strengthening method", *Struct. Monit. Maint*., **1**(3), 323-338. https://doi.org/10.12989/smm.2014.1.3.323.

Wang, B., Wu, T., Dai, H.J. and Bai, G.L. (2018), "Numerical study on the seismic performance of a steel-concrete hybrid supporting structure in thermal power plants", *Appl. Sci*., **8**(2), 294. http://dx.doi.org/10.3390/app8020294.

Wang, B., Wu, T., Dai, H.J., Bai, G.L. and Wu, J. (2019), "Pseudo-dynamic and cyclic loading tests on a steel-concrete vertical hybrid structure", *Earthq. Struct.*, **17**(4), 399-409. https://doi.org/10.12989/eas.2019.17.4.399.

Xiao, L. and Sritharan, S. (2018), "Effects of confinement in circular hollow concrete columns", *J. Struct. Eng*., **144**(9), 04018159. http://dx.doi.org/10.1061/(ASCE)ST.1943-541X.0002151.

Yeh, Y.K., Mo, Y.L. and Yang, C.Y. (2002), "Seismic performance of rectangular hollow bridge columns", *J. Struct. Eng.*, **128**(1), 60-68. http://dx.doi.org/10.1061/(ASCE)0733-9445(2002)128:1(60).

Zhao, J. and Sritharan, S. (2007), "Modeling of strain penetration effects in fiber-based analysis of reinforced Concrete Structures", *ACI Structural Journal*, **104**(2), 133-141.

GB 50011-2010 (2016), Code for seismic design of buildings, ministry of housing and urban-rural development of the people's republic of China, general administration of quality supervision, inspection and quarantine of the people's republic of China; Beijing, China.

AT